

Site-selective observation of spin dynamics of a Tomonaga-Luttinger liquid in frustrated Heisenberg chains

Diep Minh Nguyen,¹ Azimjon A. Temurjonov,¹ Daigorou Hirai,² Zenji Hiroi,³ Oleg Janson,⁴ Hiroshi Yasuoka,⁵ Taku Matsushita,¹ Yoshiaki Kobayashi,¹ and Yasuhiro Shimizu^{1,*}

¹*Department of Physics, Nagoya University, Nagoya 464-8601, Japan.*

²*Department of Applied Physics, Nagoya University, Nagoya 464-8603, Japan.*

³*Institute for Solid State Physics, University of Tokyo, Kashiwa, 277-8581, Japan.*

⁴*Institute for Theoretical Solid State Physics, Dresden, 01069, Germany.*

⁵*Max Plank Institute for Chemical Physics of Solids, 01187 Dresden, Germany.*

(Dated: February 25, 2025)

Low-energy spin dynamics is investigated by ³⁵Cl NMR measurements in a frustrated antiferromagnet Ca₃ReO₅Cl₂. The local spin susceptibility measured with the Knight shift behaves as a one-dimensional Heisenberg antiferromagnet and remains constant down to low temperatures, as expected in a gapless Tomonaga-Luttinger liquid. The nuclear spin-lattice relaxation rate T_1^{-1} demonstrates a slowing down of atomic motions and a power-law evolution of spin correlation. The Luttinger parameter is enhanced in a site-selective manner depending on the form factor of dynamical spin susceptibility. The strong anisotropy of T_1^{-1} reflects the strong spin-orbit coupling through Dzyaloshinskii-Moriya interaction. The ground state exhibits an incommensurate antiferromagnetic ordering with low-lying magnon excitations.

I. INTRODUCTION

A Tomonaga-Luttinger liquid (TLL) is characterized by fractional gapless excitations and bosonic collective modes in one-dimensional (1D) localized spin chains [1–3]. The spin correlation function of TLL follows a universal power law. One of the observables is the nuclear spin-lattice relaxation rate T_1^{-1} , which measures the dynamical spin susceptibility summed over the wave vector space in a low-energy limit. It approximately obeys the power-law temperature T dependence [4–9]:

$$T_1^{-1} \propto T^{1/2K_\sigma - 1}, \quad (1)$$

where K_σ is one of the TLL parameters. A spin-1/2 Heisenberg chain yields $K_\sigma = 1/2$, in which T_1^{-1} becomes T -invariant [10–13]. K_σ depends on the Ising anisotropy and the magnetic field strength respectively acting as the interaction and chemical potential of spinless fermions [2]. As three-dimensional (3D) coupling between the chains sets in, the system heads toward long-range magnetic ordering with the effectively enhanced K_σ above the transition temperature T_N [14, 15]. On the spin-1/2 ladder and spin-1 chain exhibiting a nonmagnetic ground state, the spin correlation measured with K_σ sensitively depends on the magnetic field [16–23].

The anisotropic triangular antiferromagnet connects 1D TLL to two-dimensional (2D) quantum spin liquid as a function of the ratio of the interchain interaction J' and the intrachain interaction J [2, 24–27]. Geometrical frustration reduces the interchain correlation and hence the system dimensionality [28, 29]. The TLL phase is

stabilized up to the exchange anisotropy $J'/J \approx 0.3$ for the interchain exchange coupling J' and the intrachain coupling J [25–30]. A spiral magnetic order occurs for $J'/J > 0.3-0.7$ on the triangular lattice. The quantum spin liquid, if any, near the isotropic point $J'/J \approx 1$ may involve a tiny spin gap and topological order [10, 31], which is distinct from the renormalized 1D liquid phase.

An example of the spin-1/2 anisotropic triangular antiferromagnets, Cs₂CuCl₄ ($J'/J = 0.3$), exhibits magnetic orders and TLL behavior with bound spinons, depending on the magnetic field strength and direction, as observed by NMR and inelastic neutron-scattering measurements [30, 32–37]. A 5d transition-metal oxychloride Ca₃ReO₅Cl₂ (CROC) is served as another example of the spin-1/2 quasi-1D antiferromagnet with the anisotropic triangular lattice, as shown in Fig. 1 [38–40]. CROC forms an orthorhombic $Pnma$ lattice, where the ReO₅ square-pyramid with the 5d_{xy} orbital forms a chain along the b axis. Despite the strong spin-orbit coupling of Re ions, the orbital moment is quenched under the asymmetric ligand field and perturbatively contributes to the ground state through the Dzyaloshinskii-Moriya (DM) interaction $\mathbf{D} \cdot \mathbf{S}_i \times \mathbf{S}_{i+1}$, where \mathbf{D} is parallel to the c axis in the ac mirror plane. The interchain coupling within the bc plane constructs an anisotropic triangular lattice, as shown in Fig. 1. The anisotropy of the triangular lattice has been evaluated as $J'/J = 0.25$ from the high-field magnetization [41], consistent with that of the calculation of density functional theory (DFT) ($J'/J = 0.295$) [39, 42]. At low temperatures, χ behaves as a spin-1/2 1D antiferromagnetic Heisenberg model with $J/k_B = 41$ K [39, 43], which implies a reduction of the dimensionality. The ground state eventually exhibits a long-range magnetic order below $T_N = 1.13$ K. Thus, one can investigate the spin correlation of the TLL state featured by K_σ in an extensive temperature range of $T_N < T < J$. Below T_N , magnon excitation may coexist with bound spinons

* Present address: Department of Physics, Shizuoka University, Shizuoka, 422-8529, Japan

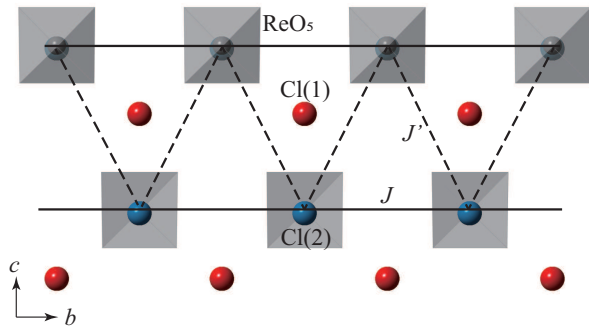


Figure 1. Crystal structure of $\text{Ca}_3\text{ReO}_5\text{Cl}_2$ ($Pnma$) without Ca atoms in a half of the unit cell along the a axis for simplicity. The intrachain interaction J and the interchain one J' are shown by the solid and dash lines, respectively. Cl(1) and Cl(2) sites are respectively located between the ReO_5 chains and on the ReO_5 pyramid, as viewed from the a axis. The symmetry operation of Re ($4c$) and two Cl sites ($4c$) are expressed in combinations of the a -glide normal to the c axis and the twofold screw along the three axes, where the fractional atomic coordinates are Re = (0.6855, 3/4, 0.0824), Cl(1) = (0.4639, 1/4, 0.2102), Cl(2) = (0.4854, 3/4, 0.4089) [38].

in the high-energy dispersion observed by the inelastic neutron scattering [44].

Here we investigate the spin excitation and structure on the quasi-1D CROC with site-selective Cl NMR spectroscopy. We determine the Knight shift and electric field gradient (EFG) tensors for two Cl sites and then compare the result with the calculation. K and T_1^{-1} measurements respectively uncover static and dynamic spin susceptibilities of CROC in the TLL regime at low temperatures. We show remarkable anisotropy and site dependence of T_1^{-1} , which are discussed in terms of the DM interaction and the wave-vector dependence of the form factor of the anisotropic dynamical spin susceptibility.

II. METHOD

The single crystals of CROC were grown by a flux method with a mixture of CaO, ReO_3 , and CaCl_2 in a quartz ampule [38]. The typical dimensions of the crystal were $0.5 \times 5 \times 2 \text{ mm}^3$. We performed ^{35}Cl and ^{37}Cl (nuclear spins $I = 3/2$) NMR measurements on a single crystal of CROC under the steady magnetic field H_0 . We utilized a dual-axis rotator for the angular dependence measurement above 1.5 K and a single-axis one in a ^3He cryostat below 1.5 K. Frequency-swept NMR spectra were obtained from spin-echo signals taken by a 0.3 MHz step using a pulse sequence $\pi/2 - \tau - \pi$ with $\pi/2 = 1.5\text{--}2.0 \mu\text{s}$ and $\tau = 50\text{--}100 \mu\text{s}$. The Knight shift K was evaluated from the central resonance frequency by subtracting the higher-order quadrupole contribution with the exact diagonalization of the nuclear-spin Hamil-

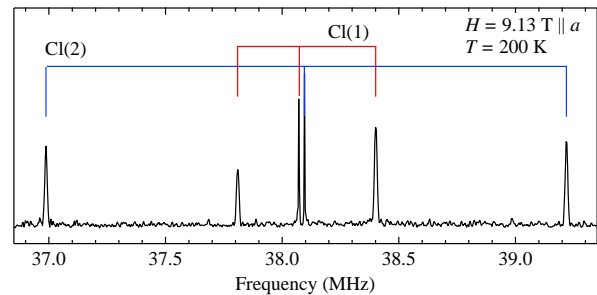


Figure 2. ^{35}Cl NMR spectrum of CROC at 200 K and $H_0 = 9.13 \text{ T}$ along the a axis. The linewidth is $\approx 2 \text{ kHz}$ for central lines. For the spectrum assignment we refer to the angular dependence of the nuclear quadrupole splitting frequency $\delta\nu$ and the central frequency shift in Appendix A.

tonian in Appendix A. The spin-lattice relaxation rate T_1^{-1} was measured with a saturation recovery method, in which nuclear magnetization $M(t)$ obeys $M(t) = M_0 - M_0 [0.1e^{-t/T_1} + 0.9e^{-6t/T_1}]$. The spin-echo decay rate T_2^{-1} was obtained from $M(2\tau) \propto \exp(-2\tau/T_2)$ for two Cl sites.

The nuclear quadrupole frequency was calculated with FPLO version 22 [45] for the standard basis (S), the extended basis (D), and the extended basis with additional $4f$ (D4f) basis sets. The values presented in the manuscript were calculated using the D4f basis, which provides the highest accuracy, on a mesh of $8 \times 16 \times 8k$ points. Relativistic effects were neglected full-relativistic calculations on sparser meshes yielded nearly identical (differing by less than 4%) quadrupole frequencies. Since there are many heavy atoms in the structure, we use the local density approximation (LDA) functional [46].

III. EXPERIMENTAL RESULTS

A. Local spin susceptibility and magnetic order

The ^{35}Cl NMR spectrum of CROC consists of extremely sharp resonance lines coming from two Cl sites, Cl(1) and Cl(2), under magnetic field along the a axis, as shown in Fig. 2. For $I = 3/2$, the spectrum from each Cl site splits into three due to the electric-quadrupole interaction between the nuclear quadrupole moment Q and the EFG at the Cl site. The number of resonance lines doubles as the inversion symmetry is broken away from the ab and bc planes, which allows us the accurate field alignment along the crystal axes within 1° . The quadrupole splitting $\delta\nu$ and the central frequency are plotted in Fig. 8 of Appendix A. The angular dependence is compared with the LDA calculation based on the crystal structure of CROC, leading to the unambiguous site assignment of the resonance lines into Cl(1) and Cl(2), as shown in Fig. 2.

The NMR spectrum displays a site-dependent shift

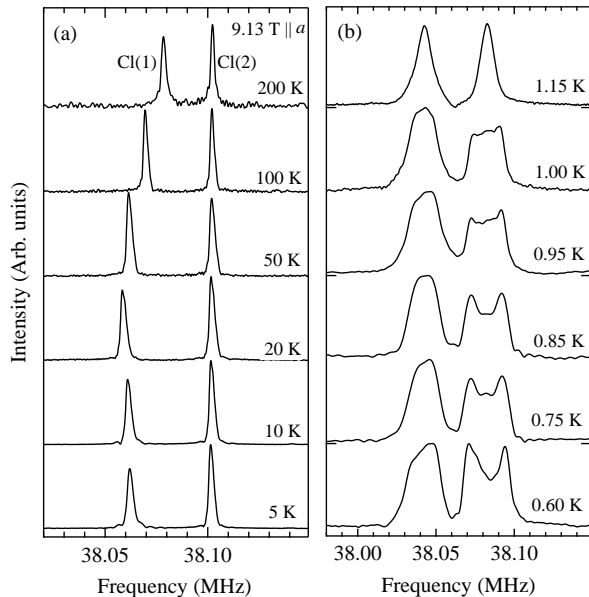


Figure 3. Temperature dependence of the central ^{35}Cl NMR spectrum for the single crystal of $\text{Ca}_3\text{ReO}_5\text{Cl}_2$ at 9.13 T along the a axis (a) above and (b) below T_N .

upon cooling, as shown in Fig. 3(a). The low-frequency spectrum from Cl(1) exhibits a downward shift, while the higher one from Cl(2) stays at nearly the same position. Since χ exhibits Curie-Weiss paramagnetic behavior at high temperatures, the downward shift indicates the negative hyperfine coupling constant for Cl(1). Surprisingly, the linewidth remains sharp down to low temperatures, indicating a high-quality crystal free from the magnetic inhomogeneity around free spins.

The Knight shift K obtained from the central resonance line scales to the local spin susceptibility χ_{ii} along the crystal i axis; $K_{ii} = \frac{A_{ii}}{N\mu_B} \chi_{ii}$ ($i = a, b, c$), where A_{ii} is the diagonal hyperfine coupling, N the Avogadro number, and μ_B the Bohr magneton. Figure 4 shows the T dependence of K for Cl(1) and Cl(2), denoted as $K(1)$ and $K(2)$, respectively. $-K(1)$ increases upon cooling, showing a broad peak around 28 K. It becomes nearly constant at low temperatures. The temperature dependence of $-K(1)$ for each crystal axis fits to the Bonner-Fisher model with $J/k_B = 38$ K ($7 < T < 70$ K) [47] in agreement with the result of χ ($J/k_B = 41.3$ K) [39]. In contrast with the bulk χ , the local spin susceptibility obtained from $K(1)$ excludes an impurity contribution and extracts the intrinsic residual spin susceptibility down to low temperatures (3.4×10^{-3} emu/mol), which corroborates the gapless TLL state. The spin susceptibility of TLL is expressed as $\chi(0) = (g\mu_B)^2 K_\sigma / (\pi v)$ using the spin velocity $v = J\pi/2$ at $T = 0$ [48, 49]. Using the T -linear term of the specific heat, $\gamma = 115$ mJ/(K mol) [39], the Wilson ratio $R_W = (\pi k_B / g\mu_B)^2 (4\chi / 3\gamma)$ is obtained as 2.46. It is compared with $R_W = 4K_\sigma$ expected for TLL spin chains [49]. Using $K_\sigma = 0.61 - 0.87$ for

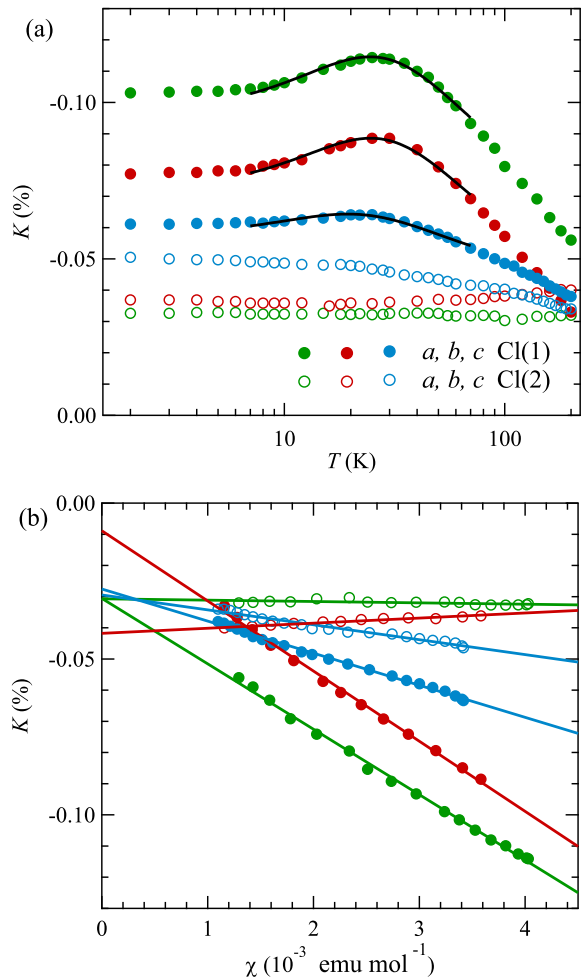


Figure 4. (a) Knight shift K measured as a function of temperature T along the crystal axes for two Cl sites. Note that the vertical axis is taken upside down. Solid curves are the Bonner-Fisher fitting with $J = 38$ K. (b) K plotted against the bulk magnetic susceptibility χ as an implicit function of T . Solid lines are linear fitting results for $T > 28$ K.

Cl(1) from T_1^{-1} as described below (Table. I), we can independently obtain $R_W = 2.44-3.48$, consistent with the Knight shift.

Since χ is nearly isotropic [39], the anisotropy of $K(1)$ comes from the anisotropic hyperfine coupling constant governed by transfer or dipole interactions. $K(1)$ linearly scales to χ above 28 K, as seen in the $K(1) - \chi$ plot [Fig. 4(b)]. The components of the hyperfine coupling tensor are evaluated from the linearity as $(A_{aa}, A_{bb}, A_{cc}, A_{ac}) = (-0.12, -0.13, -0.058, 0.13)\text{T}/\mu_B$ for Cl(1). Here, A_{ac} is evaluated from the angular dependence of Knight shifts. The diagonalization yields the principal components of the hyperfine coupling $(A_{XX}, A_{YY}, A_{ZZ}) = (0.04, -0.13, -0.22)\text{T}/\mu_B$ for Cl(1). The anisotropy is not explained by the dipolar interaction ($\sum_\alpha A_{\alpha\alpha} = 0$), and hence comes from the transferred hyperfine interaction. In contrast, $K(2)$ along the a and b axes very

weakly depends on T , indicating the tiny hyperfine coupling constants. We obtained $(A_{aa}, A_{bb}, A_{cc}, A_{ac}) = (-0.002, 0.01, -0.03, 0.14)T/\mu_B$ and $(A_{XX}, A_{YY}, A_{ZZ}) = (0.12, 0.01, -0.15)T/\mu_B$ for Cl(2). The remarkable site dependence reflects the transferred hyperfine paths originating the anisotropic Re $5d_{xy}$ orbital, as discussed in Appendixes.

Below $T_N = 1.1$ K, the NMR spectrum broadens and changes to a double horn shape, as shown in Fig. 3(b). It shows an emergence of the spontaneous local field below T_N . One can exclude a possible collinear magnetic ordering that involves a discrete splitting of the NMR spectrum by the staggered hyperfine field. Despite a hyperfine coupling constant of Cl(1) greater than Cl(2), the splitting amplitude is smaller for Cl(1) along the a axis. This means that the local fields at Cl sites are generated through the off-diagonal hyperfine coupling from the Re magnetic moments oriented perpendicular to the a axis. The double horn shape is typically observed in incommensurate magnetic orders such as corn and spiral orders [35, 50]. In the present case with strong 1D anisotropy, weakly incommensurate modulation of the wave vector can be induced by DM interactions due to the lack of inversion symmetry along the chain [41, 44]. For the D -vector \mathbf{D} parallel to the c axis, the DM interaction forces the magnetic moments to align perpendicular to \mathbf{D} . Therefore, we conclude that the moment direction should be close to the b axis.

B. Critical slowing-down of spin and atomic fluctuations

The nuclear spin-lattice relaxation rate T_1^{-1} measures low-energy excitations in the NMR frequency window through magnetic and electric hyperfine interactions. As shown in Fig. 5(a), T_1^{-1} exhibits sharp and broad peaks around 1.1 and 50 K, respectively, for $H_0 = 9.13$ T along the a axis. The sharp peak manifests the critical slowing-down of spin fluctuations toward long-range magnetic ordering at $T_N = 1.1$ K. T_1^{-1} drops steeply ($\sim T^2$) below T_N where the excitation is dominated by gapless magnons.

The broad T_1^{-1} peak around 50 K can be attributed to structural fluctuations such as atomic motions instead of phase transition, since there is no signature of symmetry breaking in the NMR spectrum (Fig. 3) and specific heat [39]. For confirmation, we measured T_1^{-1} of two isotopes ^{35}Cl and ^{37}Cl having distinct nuclear quadrupole moments $Q = -8.2$ and $-6.5 \times 10^{-26} \text{cm}^2$, respectively. As shown in Fig. 5(b), T_1^{-1} approximately scales to Q^2 around 50 K, consistent with the predominant EFG fluctuations [51].

As the resonance frequency decreases from 38 MHz at 9.13 T to 20 MHz at 4.95 T, the T_1^{-1} peak shifts to 43 K, as shown in Fig. 6(a). Further low frequency ($\sim \text{kHz}$) fluctuations can be observed through T_2^{-1} , where the spin-echo intensity decays exponentially with the pulse interval time $\tau = 100 - 1000 \mu\text{s}$. As seen from the sharp

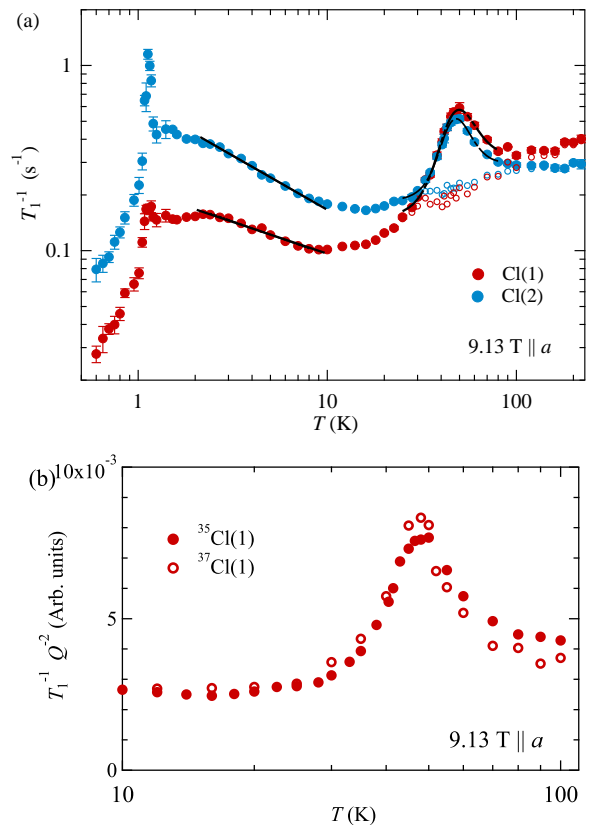


Figure 5. (a) Temperature dependence of the nuclear spin-lattice relaxation rate T_1^{-1} measured for the a axis (solid circles) for Cl(1) and Cl(2). Curves around 50 K are the BPP model fitting using Eq. (2). Open circles represent the result after subtracting the BPP contribution. Solid lines represent the power-law fitting $\sim T^{1/2K_\sigma-1}$ using the Luttinger parameter K_σ . (b) T_1^{-1} divided by the square of the nuclear quadrupole moment Q for ^{35}Cl and ^{37}Cl NMR.

resonance line, T_2 is extremely long, despite a paramagnetic Mott insulator, and reaches ~ 20 ms for Cl(1). As shown in Fig. 6(b), T_2^{-1} is independent of T above 30 K and exhibits a sharp peak at $T^* = 18$ K, indicating the freezing of atomic motions. Upon cooling, T_2^{-1} remains constant for Cl(2), while it gradually increases for Cl(1) toward the magnetic order.

From a structural point of view, the x-ray diffraction measurement on CROC shows a large thermal structure factor of Cl sites at room temperature [38]. Although the structural data of CROC are absent at low temperatures, the metastable atomic positions may induce a persistent structural instability due to the large open space. Interestingly, the structural freezing coincides with the onset of antiferromagnetic correlation, as manifested in the χ peak at 20 K.

The system crossovers from a quantum TLL regime ($T \ll J$) into a classical diffusive regime ($T \gg J$) with increasing temperature. In an intermediate temperature range of $T \sim J$, spin dynamics of 1D chains is ex-

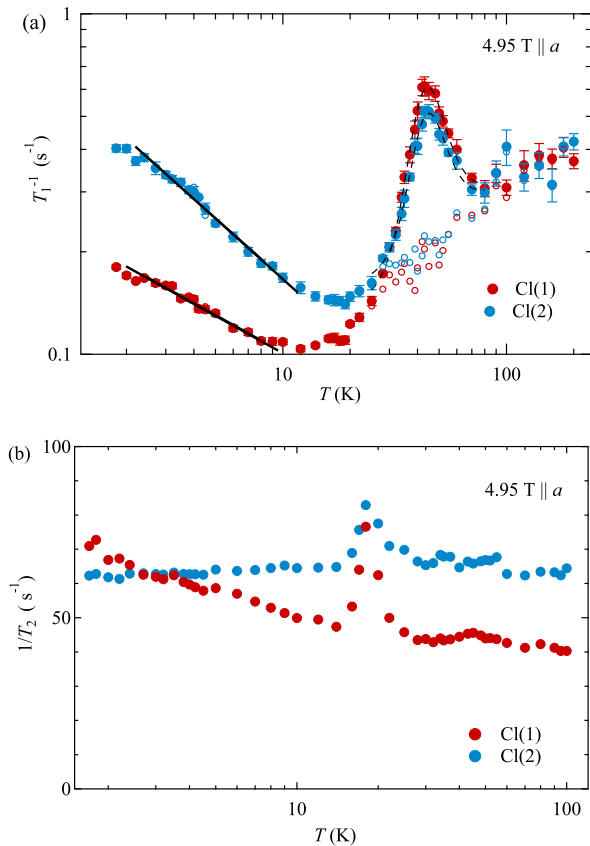


Figure 6. Temperature dependence of (a) T_1^{-1} and (b) T_2^{-1} at $H_0 = 4.95$ T along the a axis. Broken curves denote the fitting result by the BPP model using Eq.(2). Solid lines represent the power law $T_1^{-1} \propto T^{1/2K_\sigma-1}$ fitting with the Luttinger parameter K_σ .

pected to obey the superdiffusive Kardar-Parisi-Zhang (KPZ) universality with characteristic spin correlation [52, 53]. To extract the spin dynamics of the crossover regime, we subtract the structural contribution from T_1^{-1} by assuming the Lorentzian correlation function in the Bloembergen-Purcell-Pound (BPP) model [54]:

$$T_1^{-1} \propto \left[\frac{\tau_c}{1 + (\omega\tau_c)^2} + \frac{4\tau_c}{1 + (4\omega\tau_c)^2} \right], \quad (2)$$

where τ_c is the correlation time, $\tau_c = \tau_0 \exp(\frac{E_a}{k_B T})$, with the activation energy E_a and the constant τ_0 . The experimental result is well fitted by Eq. (2) at the measured frequency (38 and 20 MHz at 9.13 and 4.95 T, respectively), as shown in Figs. 5 and 6, which yields $E_a/k_B \approx 300$ K. The fitting extracts a power law $\sim T^n$ term with the exponent $n = 0.5$ in the temperature range above 20 K. It differs from those of the local spin fluctuations ($n = 0$) [55] and the KPZ universality ($n = 2$) [52, 53]. The exponent is rather close to that expected in the spin-diffusion regime of the spin-diffusion regime [56].

C. Spin dynamics in the critical TLL regime

At low temperatures ($T \ll J$), T_1^{-1} would be dominated by spin fluctuations along the chain, where structural fluctuations are exponentially suppressed. According to the fluctuation-dissipation theorem, the imaginary part of dynamical spin susceptibility $\chi(\mathbf{q})$ relates to the dynamical spin structure factor $S^\pm(\mathbf{q})$. T_1^{-1} is expressed as [50, 55, 57, 58]

$$T_{1z}^{-1} = \frac{k_B T \gamma_n^2}{2\mu_B^2 \omega} \sum_{\mathbf{q}} [(F_{xx}(\mathbf{q}) + F_{yy}(\mathbf{q}) + 2F_{xy}(\mathbf{q}))\chi''_{\perp}(\mathbf{q}) + (F_{xz}(\mathbf{q}) + F_{yz}(\mathbf{q}))\chi''_{\parallel}(\mathbf{q})] \quad (3)$$

where $F_{\alpha\beta}(\mathbf{q})$ ($\alpha, \beta = x, y, z$) is the form factor at the wave vector \mathbf{q} and defined by $F_{\alpha\beta}(\mathbf{q}) = A_{\alpha\beta}(\mathbf{q})A_{\alpha\beta}(-\mathbf{q})$ using the Fourier transformed hyperfine coupling $A_{\alpha\beta}(\mathbf{q}) = A_{\alpha\beta}(\mathbf{r})e^{i\mathbf{q}\cdot\mathbf{r}}$. χ''_{\perp} and χ''_{\parallel} are the imaginary part of the dynamical spin susceptibility perpendicular and parallel to the magnetic field. Here, the z axis is taken along the applied magnetic field direction. In 1D Mott insulators the low-energy $\chi(\mathbf{q})$ is dominated by specific wave vectors close to $\mathbf{Q}_0 = (0, \pi, 0)$ [2, 4, 10]. A shift from \mathbf{Q}_0 by the magnetic field would be negligible when the Zeeman energy is much lower than the exchange interaction J . Instead, the DM interaction induces a small splitting of the spinon dispersion by $\Delta q = 0.07\pi$ [44], which is also omitted in the following analysis for simplicity.

In a TLL regime, $\chi(\mathbf{q})$ obeys a power law in an anisotropic manner, $\chi_{\perp} \propto T^{1/2K_\sigma-2}$ and $\chi_{\parallel} \propto T^{2K_\sigma-2}$ [4, 7]. For an isotropic case, both transverse and longitudinal components of T_1^{-1} are independent of temperature ($K_\sigma = 0.5$), as expected for the antiferromagnetic Heisenberg chain [4, 10]. They become anisotropic as the Ising anisotropy Δ of the XXZ model deviates from unity. For $K_\sigma > 0.5$, the transverse component is enhanced at low temperatures, whereas the parallel component vanishes and thus becomes negligible. Furthermore, as seen from Eq. (3), χ_{\parallel} contributes to T_1^{-1} only through the off-diagonal hyperfine coupling. Therefore, T_1^{-1} would be dominated by $\chi_{\perp}(\mathbf{q})$, as shown in Eq.(1).

Below 10 K, T_1^{-1} increases with a power law $\sim T^n$, as shown in Fig. 5. The fitting yields $n = -0.36$ for Cl(1) and -0.59 for Cl(2) in a magnetic field of 9.13 T along the a axis. Applying the relation $n = 1/(2K_\sigma) - 1$ in Eq. (1), we obtained $K_\sigma = 0.79$ and 1.21 for Cl(1) and Cl(2), respectively. Since the dynamical spin susceptibility is carried by Re spins, K_σ should be independent of the probe nuclear spins. Therefore, the observed Cl site dependence comes from the form factor dependence that filters antiferromagnetic fluctuations at the specific wave vector, as typically observed in tetragonal cuprate and pnictide superconductors [11, 58].

Referring to the crystal structure of CROC in Figs. 1 and 9, Cl(1) is located between neighboring Re atoms, while Cl(2) is on the Re atom along the a axis. Here we

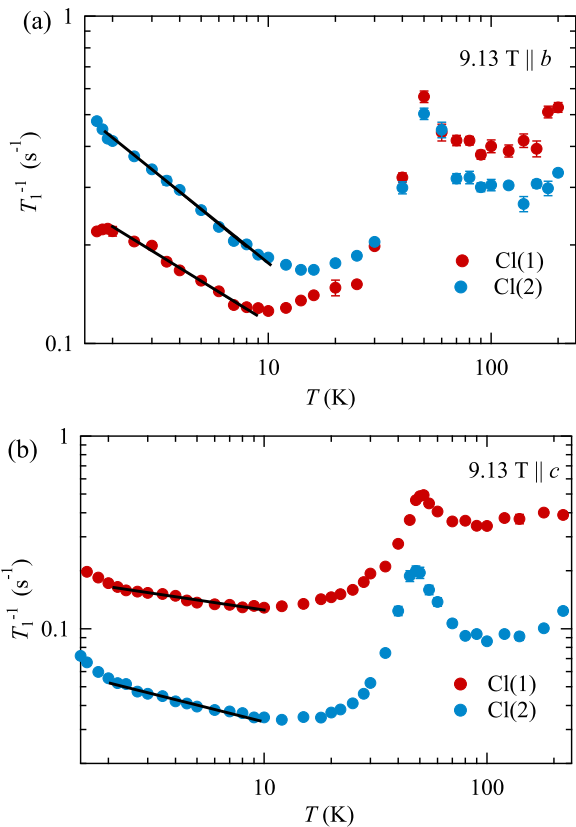


Figure 7. Temperature dependence of T_1^{-1} for $H_0 = 9.13$ T along (a) b and (b) c axes. Solid lines show the power law $T^{1/2K-1}$ fit with a parameter K_σ .

consider antiferromagnetic spin fluctuations at the wave vector $\mathbf{Q}_0 = (0, \pi, 0)$ along the chain. The staggered hyperfine fields from the second-neighbor Re sites are canceled out at Cl(1), as shown by the site-symmetry analysis in Appendix B. Then, the antiferromagnetic correlation at $\mathbf{q} = \mathbf{Q}_0$ is filtered through the form factor at Cl(1), while it remains at Cl(2). Therefore, T_1^{-1} measured at Cl(1) is strongly suppressed in contrast to that of Cl(2), despite the uniform hyperfine coupling of Cl(1) greater than that of Cl(2). T_1^{-1} is indeed reversed between Cl(1) and Cl(2) at high temperatures above 50 K, where the uniform $\mathbf{q} = 0$ mode becomes dominant.

In the TLL regime, the external magnetic field works as chemical potential and enhances magnetization or K_σ , as observed in the spin-1/2 ladder system with the spin gap [15]. We have investigated the field dependence of K_σ for the Cl sites at $H_0 = 4.95$ T, as shown in Fig. 6. There is no significant field effect on K_σ , consistent with the negligible effect of the Zeeman energy in the gapless TLL, as listed in Table I. Instead, the energy scale of the DM interaction is comparable to the magnetic field and thus impacts on the anisotropy.

Table I. TLL parameter K_σ for Cl(1) and Cl(2) under the different magnetic field orientation and strength. The values in the parentheses are obtained after the RPA analysis [14, 15].

	Cl(1)	Cl(2)
$H \parallel a, 9$ T	0.79 (0.7)	1.21 (1.0)
$H \parallel b, 9$ T	0.87 (0.7)	1.13 (1.0)
$H \parallel c, 9$ T	0.61 (0.5)	0.70 (0.6)
$H \parallel a, 5$ T	0.79	1.20

D. Anisotropy of T_1^{-1}

Finally, we investigate the anisotropy of T_1^{-1} by applying the magnetic field $H_0 = 9.13$ T along the b and c axes, as shown in Fig. 7. The result along the b axis is similar to that for the a axis in Figs. 5(a) and 6, where T_1^{-1} is dominated by atomic fluctuations at high temperatures and then by electric spin fluctuations below 20 K. At low temperatures, we obtain $K_\sigma = 0.87$ and 1.13 for Cl(1) and Cl(2), respectively, as listed in Table I. In contrast, the anisotropy of T_1^{-1} for the c axis is not reversed at low temperatures, suggesting that the $\mathbf{q} = \mathbf{Q}_0$ mode is less dominant in T_1^{-1} for Cl(1) and Cl(2). Interestingly, T_1^{-1} remains anisotropic in the intermediate temperature range where T_1^{-1} exhibits the broad peak. It may indicate significant spin-lattice coupling through the DM interaction. In the TLL regime below 20 K, we obtained K_σ , 0.61 for Cl(1) and 0.70 for Cl(2), which is much lower than those in the other directions. The reason can be attributed to the anisotropy of dynamical spin susceptibility, as discussed below.

IV. DISCUSSION

The enhancement of K_σ might be interpreted as the repulsive interaction of spinless fermions based on the XXZ model. In the present system showing isotropic spin susceptibility, the effective spin Hamiltonian would be close to the Heisenberg model with $\Delta \sim 1$. Therefore, the large K_σ for Cl(2) will originate in the antiferromagnetic correlation toward T_N , which is not taken into account within the simple TLL theory.

In the critical regime, the transverse component of T_1^{-1} is expected to follow the power law against reduced temperature, $\sim (T - T_N)^{-\nu(z_t - D - \eta_t + 2)}$, within the dynamical scaling hypothesis [14, 59], where ν is the correlation length exponent, z_t the dynamical exponent, D the dimensionality, and η_t the anomalous exponent. The exponents depend on the universality: e.g. a mean field and a 2D XY model yield $n = -0.5$ and -0.67 , respectively. Approaching T_N , the system exhibits a crossover from 1D to 3D regime, leading to the nominal enhancement of K_σ .

The effect of critical spin fluctuations on T_1^{-1} can be

calculated from the random phase approximation (RPA) below 10 K [14, 15]. A fitting into our experimental result reduces K_σ , as listed in Table I. The value is still close to unity for Cl(2). The result implies that critical spin fluctuations can be reproduced beyond the mean-field approximation near T_N .

The anisotropy of T_1^{-1} can be explained in terms of spinon dynamics under the DM interaction $\mathbf{D} \cdot \mathbf{S}_i \times \mathbf{S}_{i+1}$. In CROC, the DM vector \mathbf{D} is directed along the c axis within the mirror plane. Spinon dispersion splits by $\pi D/2 = 310$ GHz at $q = 0$ or π along the chain, as observed by the EPR measurement [41]. The excitation branches split with increasing the magnetic field strength along the c axis, whereas they monotonically increase with magnetic field along the a and b axes. The DM interaction induces the magnetic order with the moments directed within the ab plane. As a result, antiferromagnetic fluctuations are enhanced when the magnetic field is applied to the ab plane, while they are suppressed under the field along the c axis where the effect of DM interaction is minimized. Therefore, the critical spin fluctuations are largely suppressed for the c axis, which extracts the intrinsic K_σ of the TLL regime.

The field dependence of K_σ differs from that of the spin-ladder system with the gapped ground state [15, 18, 19]. The magnetic field induces the paramagnetic or long-range order phase where the effect of the DM interaction may not be negligible. However, detailed angular dependence measurements of spin fluctuations are absent. Our determination of the TLL parameter through the T_1^{-1} anisotropy measurement will promote further theoretical studies on the anisotropic hydrodynamics of quasi-1D quantum liquids.

V. CONCLUSION

We have investigated the magnetic ground state and the anisotropic low-energy excitation through the ^{35}Cl NMR measurement on the quasi-one-dimensional antiferromagnet $\text{Ca}_3\text{ReO}_5\text{Cl}_2$ with the DM interaction. We determined the nuclear quadrupole splitting and Knight shift tensors by the angular dependence of the ^{35}Cl NMR spectrum in agreement with the LDA calculation. The nuclear spin-lattice and spin-spin relaxation rates show slow atomic dynamics in the intermediate temperature range. We observed a power-law devolution of spin correlation, characteristic of one-dimensional quantum liquid. The site and angular dependence of the Luttinger parameter comes from the form-factor filtering of the antiferromagnetic correlation induced by the DM interaction. The incommensurate magnetic order occurs below 1 K with the low-lying magnon excitation.

ACKNOWLEDGEMENTS

We thank a technical support from T. Jinno and useful discussion with H. Yoshioka, S. Capponi, and N. Shannon. We acknowledge the financial support from Grant-in-aid in scientific research by JSPS (No.19H05824, 22H05256, 23H04025, 24H00954, 20H05150, 22H01178, 22H04462).

Appendix A: Nuclear quadrupole splitting

In this section, we show a complete set of the angular dependence of nuclear quadrupole splitting $\delta\nu$, which is compared with the DFT calculation.

The nuclear spin Hamiltonian is expressed as a sum of the magnetic Zeeman interaction and the electric quadrupole interaction \mathcal{H}_Q :

$$\mathcal{H} = \mathcal{H}_Z + \mathcal{H}_Q, \quad (\text{A1})$$

where the Zeeman term is given by

$$\mathcal{H}_Z = \gamma \hbar \mathbf{I} \cdot (\mathbf{H}_0 + \mathbf{H}_{\text{hf}}) \quad (\text{A2})$$

The hyperfine field is given by $\mathbf{H}_{\text{hf}} = \mathbf{K} \cdot \mathbf{H}_0$ with the Knight shift tensor \mathbf{K} . The nuclear quadrupole interaction is given by

$$\mathcal{H}_Q = \sum_{\alpha, \beta} \frac{1}{9} \delta\nu_{\alpha\beta} \left[\frac{3}{2} (I_\alpha I_\beta + I_\beta I_\alpha) - \delta_{\alpha\beta} I^2 \right], \quad (\text{A3})$$

where the nuclear quadrupole splitting $\delta\nu_{\alpha\beta}$ is defined by

$$\delta\nu_{\alpha\beta} = \frac{3eQV_{\alpha\beta}}{2I(2I-1)\hbar} \quad (\text{A4})$$

with the electric field gradient (EFG) $V_{\alpha\beta}$ and the nuclear quadrupole moment Q . Under an intense magnetic field, the ^{35}Cl ($I = 3/2$) NMR spectrum splits into three by the interval frequency $\delta\nu_{\alpha\beta}$.

The second-order electric quadrupole interaction gives a frequency shift of the central $1/2 \leftrightarrow -1/2$ transition in the order of $\nu_Q^2/\gamma_n H_0$. The satellite lines from the $3/2 \leftrightarrow 1/2$ and $-1/2 \leftrightarrow -3/2$ transitions shift equally by the second-order effect. We obtain $\delta\nu_{\alpha\beta}$ by subtracting the lowest satellite frequency from the highest one.

We measured the angular dependence of $\delta\nu_{\alpha\beta}$ about three crystal axes at 20 K and 9.13 T, as shown in Fig. 8. Without detailed analysis below, the profiles of the experimental result in Figs. 8(a,b,c) agree well with those of the LDA calculation in Figs. 8(d,e,f). Thus, we can successfully assign the ^{35}Cl NMR spectra to two Cl sites with different local environment.

Since both Cl sites are located on the mirror plane normal to the b axis, the b axis must be one of the principal axes of the EFG tensor [60, 61]. Thus, there is only one set of the spectrum from each Cl site, when we rotate the sample in the crystal plane including the b axis. Then the

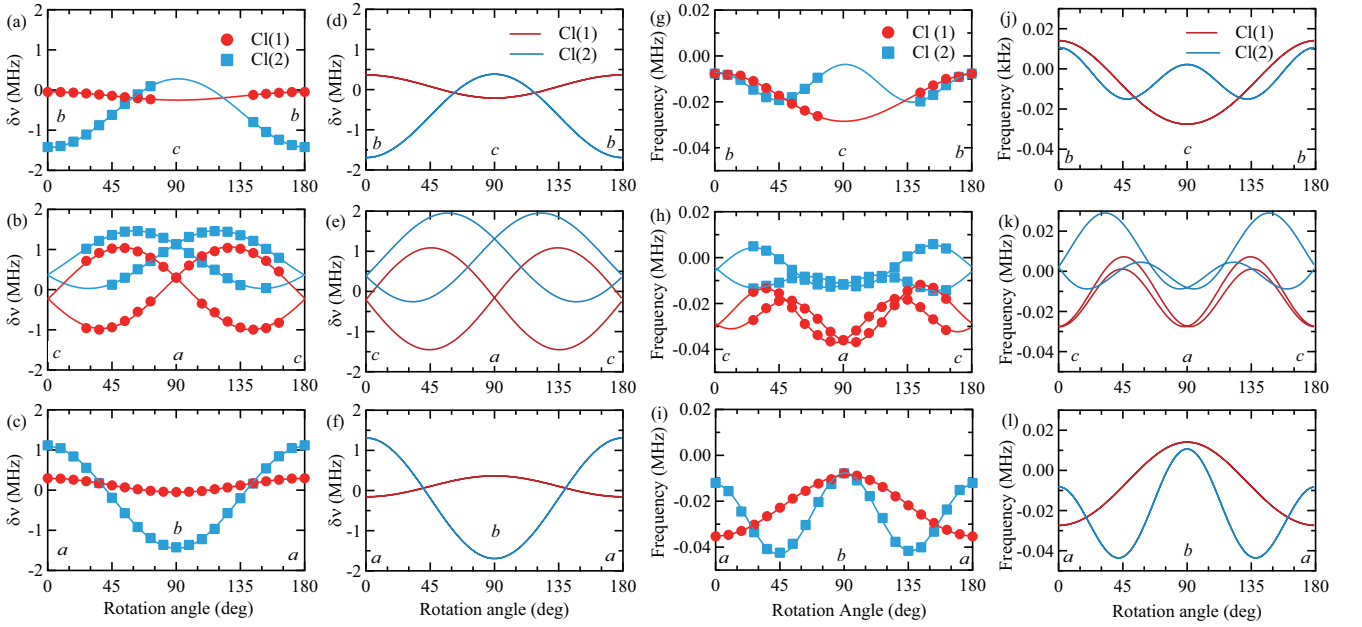


Figure 8. (a-c) Angular dependence of the nuclear quadrupole splitting frequency $\delta\nu$ for two Cl sites at 200 K. The field was rotated along the crystal axis. Solid lines show fitting to Eq. (A5). (d-f) Calculated $\delta\nu$ using LDA. (g-i) Angular dependence of the central frequency for two Cl sites at 200 K. The field was rotated about the crystal axis. Solid curves show fitting to the exact diagonalization calculation of the nuclear spin Hamiltonian including the electric quadrupole interaction and the Zeeman interaction, yielding the Knight shift tensor. (j-l) The second-order quadrupole contribution to the central frequency, obtained from the EFG calculation using the LDA functional.

off-diagonal terms vanish in the $\delta\nu_{\alpha\beta}$ tensor: $\delta\nu_{ab} = \delta\nu_{ba} = 0$, $\delta\nu_{bc} = \delta\nu_{cb} = 0$.

The number of NMR lines doubles in the ca -plane rotation about the b axis without the spatial inversion symmetry. The rotation about the b axis is analyzed with the Volkoff formula [62, 63]. On the ac -plane rotation with the angle θ_b measured from the a axis, $\delta\nu_b$ is fitted by

$$\delta\nu_b = \delta\nu_{1,b} + \delta\nu_{2,b} \cos(2\theta_b) + \delta\nu_{3,b} \sin(2\theta_b), \quad (\text{A5})$$

where the fitting coefficients are given by

$$\begin{aligned} \delta\nu_{1,b} &= (\delta\nu_{aa} + \delta\nu_{cc})/2 \\ \delta\nu_{2,b} &= (\delta\nu_{aa} - \delta\nu_{cc})/2 \\ \delta\nu_{3,b} &= -\delta\nu_{ac}. \end{aligned} \quad (\text{A6})$$

Thus, we obtained $\delta\nu_{\alpha\alpha}$ ($\alpha = a, b, c$) for each crystal axis and the off-diagonal element $\delta\nu_{ac}$, as listed in Table II. The diagonalization of the tensor yields the principal components $\delta\nu_{\alpha\alpha}$ ($\alpha = X, Y, Z$) and the asymmetric factor $\eta = |\delta\nu_{XX} - \delta\nu_{YY}|/\delta\nu_{ZZ}$, where X, Y , and Z are defined by satisfying $|\delta\nu_{XX}| < \delta\nu_{YY} < |\delta\nu_{ZZ}|$. The results are compared with the LDA calculation based on the electronic structure of CROC in Figs. A(d-f) and Table. III. Then We can obtain the quadrupole frequency $\nu_Q = \delta\nu_{ZZ}$:

$$\nu_Q = \frac{3eQV_{ZZ}}{2I(2I-1)\hbar}, \quad (\text{A7})$$

where V_{ZZ} the principal component of the diagonalized electric field gradient tensor [51].

Table II. Nuclear quadrupole splitting frequency $\delta\nu_{\alpha\alpha}$ determined from the angular dependence of the ^{35}Cl NMR spectrum at 200 K. The tensor for the crystal coordinate (a, b, c) is diagonalized with the principal axes (X, Y, Z). The asymmetry factor η is defined in the text. The Y axis for Cl(1) (or Cl(2)) is directed at $\pm 37^\circ$ ($\pm 30^\circ$) from the a axis in the ac plane.

	$\delta\nu_{aa}$	$\delta\nu_{bb}$	$\delta\nu_{cc}$	$\delta\nu_{ac}$	$\delta\nu_{XX}$	$\delta\nu_{YY}$	$\delta\nu_{ZZ}$	η
Cl(1)	0.29	-0.05	-0.24	± 0.98	0.05	0.99	-1.04	0.90
Cl(2)	1.09	-1.45	0.36	± 0.61	0.02	1.43	-1.45	0.98

Table III. Nuclear quadrupole splitting $\delta\nu_{\alpha\alpha}$ obtained from the LDA calculation for CROC. The Y (Z) axis for Cl(1) (or Cl(2)) is directed at $\pm 40^\circ$ ($\pm 33^\circ$) from the a axis in the ac plane.

	$\delta\nu_{aa}^{cal}$	$\delta\nu_{bb}^{cal}$	$\delta\nu_{cc}^{cal}$	$\delta\nu_{ac}^{cal}$	$\delta\nu_{XX}^{cal}$	$\delta\nu_{YY}^{cal}$	$\delta\nu_{ZZ}^{cal}$	η^{cal}
Cl(1)	0.47	0.05	-0.52	± 1.27	0.05	1.34	-1.39	0.92
Cl(2)	1.29	-1.71	0.36	± 1.00	-0.22	-1.71	1.93	0.77

The angular dependence of the central resonance ($-1/2 \leftrightarrow +1/2$) frequency is shown in Figs. 8(g-i) and compared to the second-order nuclear quadrupole effect obtained from the LDA calculation in Figs. 8(k-l). The good agreement between the experimental result and the calculation allows the site assignment for the two Cl sites.

Then we obtained the Knight shift tensor \mathbf{K} after subtracting the second-order quadrupole contribution by the exact diagonalization of the nuclear spin Hamiltonian of Eq.(A2).

We obtained the Knight shift tensor \mathbf{K} arising from the hyperfine interaction with Re electron spins at 200 K:

$$\mathbf{K} = \begin{pmatrix} K_{aa} & 0 & K_{ac} \\ 0 & K_{bb} & 0 \\ K_{ca} & 0 & K_{cc} \end{pmatrix} = \begin{pmatrix} -0.056 & 0 & -0.002 \\ 0 & -0.041 & 0 \\ -0.002 & 0 & -0.039 \end{pmatrix}, \begin{pmatrix} -0.032 & 0 & -0.001 \\ 0 & -0.033 & 0 \\ -0.001 & 0 & -0.033 \end{pmatrix}$$

in % for Cl(1) and Cl(2), respectively. The diagonalization of the tensor yields $(K_{XX}, K_{YY}, K_{ZZ}) = (-0.039, -0.041, -0.056)\%$ for Cl(1) and $(-0.032, -0.033, -0.033)$ for Cl(2), where Z is directed at $\pm 7^\circ$ and $\pm 71^\circ$ from the a axis in the ac plane, respectively. We also calculated the magnetic dipole field at Cl sites from Re ions. However, the result disagrees with the experimental result, which indicates that the Knight shift is governed by the transferred hyperfine coupling through the oxygen and calcium ions. Therefore, the hyperfine coupling does not necessarily scale to the atomic distances but depends on the paths through the overlap between the wavefunctions. The following discussion for the form factor is independent of the numerical value of the hyperfine coupling.

Appendix B: Form factors of dynamical spin susceptibility

To explain the site dependence of T_1^{-1} , we evaluated the form factor of the dynamical spin susceptibility using the symmetry operation in the crystal structure of CROC [38]. As shown in Fig. 1, Cl(1) and Cl(2) sites are located between Re ions and on the Re ion, respectively. Here we focus on the original Cl sites with the fractional coordinate of the $Pnma$ $4c$ position, (x_1, y_1, z_1) , $y_1 = 1/4$, and the surrounding Re sites ($4c$). Then we semi-quantitatively evaluate the hyperfine coupling based on the local symmetry.

For Cl(1), there are one first neighbor Re site (3.716\AA), $\text{Re}_1^{(1)}$, two second ones (4.094\AA), $\text{Re}_1^{(2)}$ and $\text{Re}_1^{(2')}$, two third ones (4.892\AA), $\text{Re}_1^{(3)}$ and $\text{Re}_1^{(3')}$, and one fourth one (5.868\AA) $\text{Re}_1^{(4)}$. The fractional coordinates of Re are given by $\text{Re}_1^{(1)} = (-x + 1, -y + 1, 0)$, $\text{Re}_1^{(2)} = (x, y, z)$, $\text{Re}_1^{(2')} = (x, y - 1, z)$, $\text{Re}_1^{(3)} = (x + 1/2, y, -z + 1/2)$, $\text{Re}_1^{(3')} = (x + 1/2, y - 1, -z + 1/2)$, and $\text{Re}_1^{(4)} = (-x + 3/2, -y + 1, z + 1/2)$, where $y = 3/4$. The relative vectors of the Cl(1)- $\text{Re}_1^{(i)}$ bonds are thus written as $\mathbf{r}_1^{(1)} = (1 - x - x_1, 0, -z - z_1)$, $\mathbf{r}_1^{(2)} = (x - x_1, 1/2, z - z_1)$, $\mathbf{r}_1^{(2')} =$

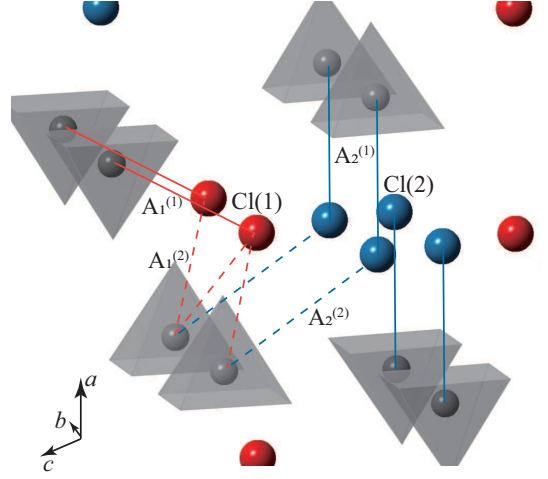


Figure 9. Geometry of hyperfine interaction between Cl nuclear spins and Re sites in $\text{Ca}_3\text{ReO}_5\text{Cl}_2$. Solid and dashed lines indicate nearest and next nearest Re-Cl bonds.

$(x - x_1, -1/2, z - z_1)$, $\mathbf{r}_1^{(3)} = (x - 1/2 - x_1, 1/2, -z + 1/2 - z_1)$, $\mathbf{r}_1^{(3')} = (x - 1/2 - x_1, -1/2, -z + 1/2 - z_1)$, and $\mathbf{r}_1^{(4)} = (-x - 3/2 - x_1, 0, z + 1/2 - z_1)$. Here $\text{Re}_1^{(2)}$ and $\text{Re}_1^{(2')}$ are connected via mirror reflection normal to the ac plane on Cl(1).

Thus the hyperfine coupling tensor can be expressed as

$$\mathbf{A}_1^{(1)} = \begin{pmatrix} A_{1aa}^{(1)} & 0 & A_{1ac}^{(1)} \\ 0 & A_{1bb}^{(1)} & 0 \\ A_{1ca}^{(1)} & 0 & A_{1cc}^{(1)} \end{pmatrix} \quad (\text{B1})$$

$$\mathbf{A}_1^{(2)} = \begin{pmatrix} A_{1aa}^{(2)} & A_{1ab}^{(2)} & A_{1ac}^{(2)} \\ A_{1ba}^{(2)} & A_{1bb}^{(2)} & A_{1bc}^{(2)} \\ A_{1ca}^{(2)} & A_{1cb}^{(2)} & A_{1cc}^{(2)} \end{pmatrix}$$

$$\mathbf{A}_1^{(2')} = \begin{pmatrix} A_{1aa}^{(2)} & -A_{1ab}^{(2)} & A_{1ac}^{(2)} \\ -A_{1ba}^{(2)} & A_{1bb}^{(2)} & -A_{1bc}^{(2)} \\ A_{1ca}^{(2)} & -A_{1cb}^{(2)} & A_{1cc}^{(2)} \end{pmatrix}. \quad (\text{B2})$$

$\mathbf{A}^{(3)}$, $\mathbf{A}^{(3')}$, and $\mathbf{A}^{(4)}$ are written similar to $\mathbf{A}^{(2)}$, $\mathbf{A}^{(2')}$, and $\mathbf{A}^{(1)}$, respectively. The net hyperfine coupling tensor is expressed as a sum of the hyperfine paths, $\mathbf{A}_1 = \sum_i \mathbf{A}_1^{(i)}$. Taking Fourier transformation

$$\mathbf{A}_1(\mathbf{q}) = \sum_i \mathbf{A}_1^{(i)}(\mathbf{r}_i) e^{i\mathbf{q}\cdot\mathbf{r}_i}, \quad (\text{B3})$$

we obtain the uniform mode of the hyperfine coupling tensor for Cl(1)

$$\mathbf{A}_1(\mathbf{0}) \simeq \begin{pmatrix} A_{1aa}^{(1)} + 2A_{1aa}^{(2)} & 0 & A_{1ac}^{(1)} + 2A_{1ac}^{(2)} \\ 0 & A_{1bb}^{(1)} + 2A_{1bb}^{(2)} & 0 \\ A_{1ca}^{(1)} + 2A_{1ca}^{(2)} & 0 & A_{1cc}^{(1)} + 2A_{1cc}^{(2)} \end{pmatrix}$$

where we omit the higher order terms for simplicity. The staggered mode along the b axis with the specific wave

vector $\mathbf{Q}_0 = (0, \pi, 0)$ is expected to dominate the low-energy spin correlation in the 1D chain. The hyperfine tensor at \mathbf{Q}_0 is calculated as

$$\mathbf{A}_1(\mathbf{Q}_0) \simeq \begin{pmatrix} A_{1aa}^{(1)} & 2iA_{1ab}^{(2)} & A_{1ac}^{(1)} \\ 2iA_{1ba}^{(2)} & A_{1bb}^{(1)} & 2iA_{1bc}^{(2)} \\ A_{1ca}^{(1)} & 2iA_{1cb}^{(2)} & A_{1cc}^{(1)} \end{pmatrix}.$$

The second neighbor interactions remain for $\mathbf{A}_1(\mathbf{0})$ but vanished for $\mathbf{A}_1(\mathbf{Q}_0)$ in the diagonal components. Namely, antiferromagnetic spin fluctuations are partly filtered through the hyperfine form factor at Cl(1).

As for Cl(2) = (x_2, y_2, z_2) , $y_2 = 3/4$, there are one nearest neighbor (3.555Å) and one second neighbor (4.350Å) Re site. We omit the higher order terms with the distance exceeding 5 Å. Similar to Cl(1), the Cl(2)-Re vectors are

expressed as $\mathbf{r}_2^{(1)} = (x - 1/2 - x_2, 0, -z + 1/2 - z_2)$ and $\mathbf{r}_2^{(2)} = (x - x_2, 0, z - z_2)$. Thus both the uniform and staggered mode of the hyperfine coupling tensor $\mathbf{A}(\mathbf{q})$ ($\mathbf{q} = \mathbf{0}, \mathbf{Q}_0$) is expressed as

$$\mathbf{A}_2(\mathbf{q}) \simeq \begin{pmatrix} A_{2aa}^{(1)} + A_{2aa}^{(2)} & 0 & A_{2ac}^{(1)} + A_{2ac}^{(2)} \\ 0 & A_{2bb}^{(1)} + A_{2bb}^{(2)} & 0 \\ A_{2ca}^{(1)} + A_{2ca}^{(2)} & 0 & A_{2cc}^{(1)} + A_{2cc}^{(2)} \end{pmatrix}.$$

The hyperfine form factor along the field direction, F_{\parallel} is calculated as $F_{\parallel} = \sum_{\alpha} A_{\alpha\beta}(q)A_{\alpha\beta}(-q)$. For $r_1^{(1)} > r_2^{(1)}$, $A_{2\alpha\beta}^{(1)}$ is greater than $A_{1\alpha\beta}^{(1)}$. Since the staggered spin fluctuations at \mathbf{Q}_0 are dominant at low temperatures, the reversed T_1^{-1} values of Cl(1) and Cl(2) can be attributed to the partial cancellation of the form factor at Cl(1) due to the antisymmetric spin fluctuations at the second neighbor Re spins.

-
- [1] F. D. M. Haldane, J. Phys. C: Solid State Phys. **14**, 2585 (1981).
- [2] T. Giamarchi, *Quantum physics in one dimension* (Oxford Univ. Press, 2003).
- [3] S. Sachdev, *Quantum Phase Transitions*, 2nd ed. (Cambridge University Press, 2011).
- [4] R. Chitra and T. Giamarchi, Critical properties of gapped spin-chains and ladders in a magnetic field, Phys. Rev. B **55**, 5816 (1997).
- [5] M. Bocquet, F. H. L. Essler, A. M. Tsvelik, and A. O. Gogolin, Finite-temperature dynamical magnetic susceptibility of quasi-one-dimensional frustrated spin- $\frac{1}{2}$ Heisenberg antiferromagnets, Phys. Rev. B **64**, 094425 (2001).
- [6] T. Hikihara and A. Furusaki, Spin correlations in the two-leg antiferromagnetic ladder in a magnetic field, Phys. Rev. B **63**, 134438 (2001).
- [7] M. Sato, T. Momoi, and A. Furusaki, NMR relaxation rate and dynamical structure factors in nematic and multipolar liquids of frustrated spin chains under magnetic fields, Phys. Rev. B **79**, 060406 (2009).
- [8] M. Sato, T. Hikihara, and T. Momoi, Field and temperature dependence of NMR relaxation rate in the magnetic quadrupolar liquid phase of spin- $\frac{1}{2}$ frustrated ferromagnetic chains, Phys. Rev. B **83**, 064405 (2011).
- [9] E. Coira, P. Barmettler, T. Giamarchi, and C. Kollath, Temperature dependence of the NMR spin-lattice relaxation rate for spin- $\frac{1}{2}$ chains, Phys. Rev. B **94**, 144408 (2016).
- [10] S. Sachdev, NMR relaxation in half-integer antiferromagnetic spin chains, Phys. Rev. B **50**, 13006 (1994).
- [11] M. Takigawa, A. P. Reyes, P. C. Hammel, J. D. Thompson, R. H. Heffner, Z. Fisk, and K. C. Ott, Cu and O nmr studies of the magnetic properties of YBa₂Cu₃O_{6.63} ($T_c=62$ K), Phys. Rev. B **43**, 247 (1991).
- [12] M. Takigawa, N. Motoyama, H. Eisaki, and S. Uchida, Dynamics in the $S = 1/2$ one-dimensional antiferromagnet Sr₂CuO₃ via ⁶³Cu NMR, Phys. Rev. Lett. **76**, 4612 (1996).
- [13] K. R. Thurber, A. W. Hunt, T. Imai, and F. C. Chou, ¹⁷O NMR study of $q = 0$ spin excitations in a nearly ideal $S = \frac{1}{2}$ 1D Heisenberg antiferromagnet, Sr₂CuO₃, up to 800 K, Phys. Rev. Lett. **87**, 247202 (2001).
- [14] M. Dupont, S. Capponi, N. Laflorencie, and E. Orignac, Dynamical response and dimensional crossover for spatially anisotropic antiferromagnets, Phys. Rev. B **98**, 094403 (2018).
- [15] M. Horvatić, M. Klanjšek, and E. Orignac, Direct determination of the Tomonaga-Luttinger parameter K in quasi-one-dimensional spin systems, Phys. Rev. B **101**, 220406 (2020).
- [16] T. Giamarchi and A. M. Tsvelik, Coupled ladders in a magnetic field, Phys. Rev. B **59**, 11398 (1999).
- [17] K. R. Thurber, T. Imai, T. Saitoh, M. Azuma, M. Takano, and F. C. Chou, ⁶³Cu NQR evidence of dimensional crossover to anisotropic 2D regime in $S = \frac{1}{2}$ three-leg ladder Sr₂Cu₃O₅, Phys. Rev. Lett. **84**, 558 (2000).
- [18] M. Klanjšek, H. Mayaffre, C. Berthier, M. Horvatić, B. Chiari, O. Piovesana, P. Bouillot, C. Kollath, E. Orignac, R. Citro, and T. Giamarchi, Controlling Luttinger liquid physics in spin ladders under a magnetic field, Phys. Rev. Lett. **101**, 137207 (2008).
- [19] P. Bouillot, C. Kollath, A. M. Läuchli, M. Zvonarev, B. Thielemann, C. Rüegg, E. Orignac, R. Citro, M. Klanjšek, C. Berthier, M. Horvatić, and T. Giamarchi, Statics and dynamics of weakly coupled antiferromagnetic spin- $\frac{1}{2}$ ladders in a magnetic field, Phys. Rev. B **83**, 054407 (2011).
- [20] S. Mukhopadhyay, M. Klanjšek, M. S. Grbić, R. Blinder, H. Mayaffre, C. Berthier, M. Horvatić, M. A. Continentino, A. Paduan-Filho, B. Chiari, and O. Piovesana, Quantum-critical spin dynamics in quasi-one-dimensional antiferromagnets, Phys. Rev. Lett. **109**, 177206 (2012).
- [21] M. Jeong, D. Schmidiger, H. Mayaffre, M. Klanjšek, C. Berthier, W. Knafo, G. Ballon, B. Vignolle, S. Krämer, A. Zheludev, and M. Horvatić, Dichotomy between attractive and repulsive Tomonaga-Luttinger liquids in spin ladders, Phys. Rev. Lett. **117**, 106402 (2016).

- [22] J. S. Möller, T. Lancaster, S. J. Blundell, F. L. Pratt, P. J. Baker, F. Xiao, R. C. Williams, W. Hayes, M. M. Turnbull, and C. P. Landee, Quantum-critical spin dynamics in a Tomonaga-Luttinger liquid studied with muon-spin relaxation, *Phys. Rev. B* **95**, 020402 (2017).
- [23] M. Dupont, S. Capponi, and N. Laflorencie, Temperature dependence of the NMR relaxation rate $1/T_1$ for quantum spin chains, *Phys. Rev. B* **94**, 144409 (2016).
- [24] S. Sachdev, T. Senthil, and R. Shankar, Finite-temperature properties of quantum antiferromagnets in a uniform magnetic field in one and two dimensions, *Phys. Rev. B* **50**, 258 (1994).
- [25] S. Yunoki and S. Sorella, Two spin liquid phases in the spatially anisotropic triangular Heisenberg model, *Phys. Rev. B* **74**, 014408 (2006).
- [26] D. Heidarian, S. Sorella, and F. Becca, Spin- $\frac{1}{2}$ Heisenberg model on the anisotropic triangular lattice: From magnetism to a one-dimensional spin liquid, *Phys. Rev. B* **80**, 012404 (2009).
- [27] P. Hauke, Quantum disorder in the spatially completely anisotropic triangular lattice, *Phys. Rev. B* **87**, 014415 (2013).
- [28] M. Q. Weng, D. N. Sheng, Z. Y. Weng, and R. J. Bursill, Spin-liquid phase in an anisotropic triangular-lattice heisenberg model: Exact diagonalization and density-matrix renormalization group calculations, *Phys. Rev. B* **74**, 012407 (2006).
- [29] Y. Hayashi and M. Ogata, Possibility of gapless spin liquid state by one-dimensionalization, *J. Phys. Soc. Jpn.* **76**, 053705 (2007).
- [30] O. A. Starykh and L. Balents, Ordering in spatially anisotropic triangular antiferromagnets, *Phys. Rev. Lett.* **98**, 077205 (2007).
- [31] X.-G. Wen, Quantum orders and symmetric spin liquids, *Phys. Rev. B* **65**, 165113 (2002).
- [32] R. Coldea, D. A. Tennant, A. M. Tsvelik, and Z. Tylczynski, Experimental realization of a 2D fractional quantum spin liquid, *Phys. Rev. Lett.* **86**, 1335 (2001).
- [33] R. Coldea, D. A. Tennant, and Z. Tylczynski, Extended scattering continua characteristic of spin fractionalization in the two-dimensional frustrated quantum magnet Cs_2CuCl_4 observed by neutron scattering, *Phys. Rev. B* **68**, 134424 (2003).
- [34] M. Kohno, O. Starykh, and L. Balents, Spinons and triplons in spatially anisotropic frustrated antiferromagnets., *Nat. Phys.* **3**, 790 (2007).
- [35] O. A. Starykh, H. Katsura, and L. Balents, Extreme sensitivity of a frustrated quantum magnet: Cs_2CuCl_4 , *Phys. Rev. B* **82**, 014421 (2010).
- [36] M.-A. Vachon, W. Kundhikanjana, A. Straub, V. F. Mitrović, A. P. Reyes, P. Kuhns, R. Coldea, and Z. Tylczynski, ^{133}Cs NMR investigation of 2D frustrated Heisenberg antiferromagnet, Cs_2CuCl_4 , *New J. Phys.* **8**, 222 (2006).
- [37] M.-A. Vachon, G. Koutroulakis, V. F. Mitrović, O. Ma, J. B. Marston, A. P. Reyes, P. Kuhns, R. Coldea, and Z. Tylczynski, The nature of the low-energy excitations in the short-range-ordered region of Cs_2CuCl_4 as revealed by ^{133}Cs nuclear magnetic resonance, *New J. Phys.* **13**, 093029 (2011).
- [38] D. Hirai, T. Yajima, D. Nishio-Hamane, C. Kim, H. Akiyama, M. Kawamura, T. Misawa, N. Abe, T. Arima, and Z. Hiroi, Visible $5d$ orbital states in a pleochroic oxychloride, *J. Am. Chem. Soc.* **139**, 10784 (2017).
- [39] D. Hirai, K. Nawa, M. Kawamura, T. Misawa, and Z. Hiroi, One-dimensionalization by geometrical frustration in the anisotropic triangular lattice of the $5d$ quantum antiferromagnet $\text{Ca}_3\text{ReO}_5\text{Cl}_2$, *J. Phys. Soc. Jpn.* **88**, 044708 (2019).
- [40] D. Hirai, Pinalites: Optical properties and quantum magnetism of heteroanionic $A_3\text{MO}_5\text{X}_2$ compounds, *Inorganic Chemistry* **63**, 4001 (2024).
- [41] S. A. Zvyagin, A. N. Ponomaryov, J. Wosnitzer, D. Hirai, Z. Hiroi, M. Gen, Y. Kohama, A. Matsuo, Y. H. Matsuda, and K. Kindo, Dimensional reduction and incommensurate dynamic correlations in the $S = \frac{1}{2}$ triangular-lattice antiferromagnet $\text{Ca}_3\text{ReO}_5\text{Cl}_2$, *Nat. Commun.* **13**, 6310 (2022).
- [42] Y. Choi, S. Lee, J.-H. Lee, S. Lee, M.-J. Seong, and K.-Y. Choi, Bosonic spinons in anisotropic triangular antiferromagnets, *Nat. Commun.* **12**, 6453 (2021).
- [43] W. Zheng, R. R. P. Singh, R. H. McKenzie, and R. Coldea, Temperature dependence of the magnetic susceptibility for triangular-lattice antiferromagnets with spatially anisotropic exchange constants, *Phys. Rev. B* **71**, 134422 (2005).
- [44] K. Nawa, D. Hirai, M. Kofu, K. Nakajima, R. Murasaki, S. Kogane, M. Kimata, H. Nojiri, Z. Hiroi, and T. J. Sato, Bound spinon excitations in the spin- $\frac{1}{2}$ anisotropic triangular antiferromagnet $\text{Ca}_3\text{ReO}_5\text{Cl}_2$, *Phys. Rev. Research* **2**, 043121 (2020).
- [45] K. Koepf and H. Eschrig, Full-potential nonorthogonal local-orbital minimum-basis band-structure scheme, *Phys. Rev. B* **59**, 1743 (1999).
- [46] J. P. Perdew and Y. Wang, Accurate and simple analytic representation of the electron-gas correlation energy, *Phys. Rev. B* **45**, 13244 (1992).
- [47] J. C. Bonner and M. E. Fisher, Linear magnetic chains with anisotropic coupling, *Phys. Rev.* **135**, A640 (1964).
- [48] S. Eggert, I. Affleck, and M. Takahashi, Susceptibility of the spin $1/2$ Heisenberg antiferromagnetic chain, *Phys. Rev. Lett.* **73**, 332 (1994).
- [49] K. Ninios, T. Hong, T. Manabe, C. Hotta, S. N. Herrer, M. M. Turnbull, C. P. Landee, Y. Takano, and H. B. Chan, Wilson ratio of a Tomonaga-Luttinger liquid in a spin- $1/2$ Heisenberg ladder, *Phys. Rev. Lett.* **108**, 097201 (2012).
- [50] K. Nawa, M. Takigawa, M. Yoshida, and K. Yoshimura, Anisotropic spin fluctuations in the quasi one-dimensional frustrated magnet LiCuVO_4 , *J. Phys. Soc. Jpn.* **82**, 094709 (2013).
- [51] A. Abragam and B. Bleaney, *Electron Paramagnetic Resonance of Transition Ions* (Oxford University Press, London, 1970).
- [52] J. De Nardis, M. Medenjak, C. Karrasch, and E. Ilievski, Anomalous spin diffusion in one-dimensional antiferromagnets, *Phys. Rev. Lett.* **123**, 186601 (2019).
- [53] M. Dupont, N. E. Sherman, and J. E. Moore, Spatiotemporal crossover between low- and high-temperature dynamical regimes in the quantum Heisenberg magnet, *Phys. Rev. Lett.* **127**, 107201 (2021).
- [54] N. Bloembergen, E. Purcell, and R. Pound, Nuclear magnetic relaxation., *Nature(London)* **160**, 475 (1947).
- [55] T. Moriya, Nuclear magnetic relaxation in antiferromagnetics, *Phys. Rev.* **101**, 1435 (1956).
- [56] M. Polini and G. Vignale, Spin drag and spin-charge separation in cold fermi gases,

- Phys. Rev. Lett. **98**, 266403 (2007).
- [57] C. Berthier, M. Horvatić, M.-H. Julien, H. Mayaffre, and S. Krämer, Nuclear magnetic resonance in high magnetic field: Application to condensed matter physics, *Comptes Rendus. Physique* **18**, 331 (2017).
- [58] A. Smerald and N. Shannon, Angle-resolved NMR: Quantitative theory of ^{75}As T_1 relaxation rate in BaFe_2As_2 , *Phys. Rev. B* **84**, 184437 (2011).
- [59] P. C. Hohenberg and B. I. Halperin, Theory of dynamic critical phenomena, *Rev. Mod. Phys.* **49**, 435 (1977).
- [60] Y. Shimizu, S. Aoyama, T. Jinno, M. Itoh, and Y. Ueda, Site-selective Mott transition in a quasi-one-dimensional vanadate V_6O_{13} , *Phys. Rev. Lett.* **114**, 166403 (2015).
- [61] Y. Shimizu, T. Jin-no, F. Iwase, M. Itoh, and Y. Ueda, Occupation switching of d orbitals in vanadium dioxide probed via hyperfine interactions, *Phys. Rev. B* **101**, 245123 (2020).
- [62] G. M. Volkoff, Second order nuclear quadrupole effects in single crystals: Part I. theoretical, *Can. J. Phys.* **31**, 820 (1953).
- [63] C. P. Slichter, *Principles of magnetic resonance* (Springer Berlin, Heidelberg, Berlin, 1970).